On the computation and application of exact Green's function in acoustic analogy

F. Q. Hu, Y. P. Guo[†] and A. D. Jones[‡]

*†Department of Mathematics and Statistics, Old Dominion University
Norfolk, Virginia 23529

[†]The Boeing Company, Huntington Beach, CA 92647

We present a numerical computation of exact Green's functions for their application in the theory of acoustic analogy. The this paper, the exact Green's function is defined as the solution of the convective wave equation that satisfies all solid wall boundary conditions. Our numerical method is based on the Boundary Element Method in the frequency domain. A general three dimensional cylindrical geometry with arbitrary cross section is assumed for the solid surfaces. However, the source point in the computed Green's function can be either a two-dimensional line source or a three-dimensional point source. In addition, the double divergence of the Green's function, to be used in the acoustic analogy formulation, is computed directly from the boundary element solution. It is shown that in order to compute the double divergence for field points close to the boundary, a better accuracy of the boundary element solution than what is sufficient for the Green's function itself is necessary. For this purpose, a spectral collocation method with high-order orthogonal polynomials as the basis functions is used. Exponential rate of convergence is demonstrated. Numerical solutions are compared with the known exact solutions whenever possible. Finally, an example of applying the numerically computed exact Green's function in the acoustic analogy for a turbulent flow over a circular cylinder is presented.

I. Introduction

The free space Green's function of the wave equation has been used extensively in the theory of acoustic analogy. For instance, in the Ffowcs Williams-Hawkings equation, through the use of the free space Green's function, the far field noise is expressed as the sum of surface integrals of unsteady pressure and a volume integral of turbulent sources. ^{2,7,10} This has become a very useful approach in recent airframe noise computations. ^{3,12} On the other hand, if one uses an exact, or tailored, Green's function, which satisfies the wall boundary conditions on all solid surfaces, the far field pressure fluctuation can be expressed as a single volume integral over the sound producing region. ^{5,6,11,13} The elimination of the need for unsteady surface pressure could be advantageous in developing noise prediction strategies based on steady CFD calculations. However, except for the very simple geometries, the exact Green's function has to be found numerically.

In this paper, we will study the numerical solution of the exact Green's function by the Boundary Element Method (BEM). The boundary element method is a meshless method that is well-suited for solving the wave equation with complex geometries. It also reduces the dimension of the problem by one, making it an efficient numerical tool. With this method, the mean flow has to be approximated as uniform but it can take full account of the complex geometry. This may be an acceptable approximation for airframe noise because the mean flow Mach number is usually low, of the order of 0.2, and the dominant wave propagation effects are the reflection and diffraction by the high lift system, a feature related purely to the geometry.

^{*}Professor, Senior member AIAA

[†]Technical Fellow, Senior member AIAA

[‡]Graduate student

Copyright © 2005 by the American Institute of Aeronautics and Astronautics. All rights reserved.

Numerical solution of the convective Helmholtz equation by the Boundary Element Method has been studied previously. ^{1,9,11,13,15} One of the main points of the present paper is about the the computation of the double divergence of the exact Green's function for its use in the acoustic analogy calculations. In most BEM codes in the literature, the boundary elements are often limited to constant or linear functions. This may be adequate for computing the Green' function itself. However, as we will demonstrate in this paper, in order to compute the spatial double divergence of the Green's function for flow regions close to the solid boundaries, a higher accuracy than what is sufficient for the Green's function itself is necessary. We present a spectral collocation boundary element method for the solution of the convective Helmholtz equation where orthogonal polynomials (the Chebyshev polynomials) are used as the basis functions. Furthermore, discontinuous boundary elements are used so that the order of the scheme can be increased easily. Exponential rate of convergence is achieved.

A second point of the paper is on the modeling of three-dimensional point source for cylindrical bodies. Our formulation starts with the three-dimensional convective wave equation. The general formulation is then reduced to applications where the surfaces of solid bodies can be regarded as two-dimensional, as is often the case in wind tunnel tests for aircraft slat noise where the slat brackets and other supporting structures are neglected. This differs from the standard truly two-dimensional equations, because the far field locations, corresponding to microphones, can never be two-dimensional.

The rest of the paper is organized as follows. In the next section, the boundary integral equation for the exact Green's function is formulated in three-dimensional space with cylindrical bodies. In section III, the spectral collocation method is described in detail and the treatment of kernel singularities is discussed. Numerical solutions are presented in section IV and the spectral accuracy of the method for the exact Green's function as well as its double divergence is demonstrated. An example of applying the exact Green's function in the computation of acoustic radiation generated by a turbulent flow over a circular cylinder is presented in section V. Section VI has the concluding remarks.

II. Exact Green's function and the boundary integral equation

A. Formulation of the Boundary Integral Equation

For the present paper, the exact Green's function is defined as the solution to the convective wave equation

$$\left(\frac{\partial}{\partial t} + \mathbf{U} \cdot \nabla\right)^2 g(\mathbf{x}, \mathbf{y}, t, s) - \nabla^2 g(\mathbf{x}, \mathbf{y}, t, s) = \delta(t - s)\delta(\mathbf{x} - \mathbf{y})$$
(1)

with boundary condition for its normal derivative

$$\frac{\partial g}{\partial n} = 0 \text{ on all solid surfaces } \Gamma \tag{2}$$

Here, \mathbf{y} is a fixed source point, or the far field observation point, and $\mathbf{x} = (x_1, x_2, x_3)$ is the field point for the solution. The uniform mean flow is assumed to be in the direction of x_1 with $\mathbf{U} = (M, 0, 0)$ where M is the Mach number. The exact Green's function is also referred to as the "tailored" Green's function, 6 as it is specific to the geometry of the acoustic problem under investigation. When \mathbf{y} is a far field observation point, the adjoint equation of (1) is implied with \mathbf{U} replaced by $-\mathbf{U}$. Throughout this paper, the bold face letters indicate vectors or matrices.

We will find the solution of (1) in the frequency domain. After a Fourier transform in time, the equation for the frequency domain Green's function $\tilde{g}(\mathbf{x}, \mathbf{y}, \omega, s)$ is

$$(-i\omega + \mathbf{U} \cdot \nabla)^2 \tilde{g} - \nabla^2 \tilde{g} = e^{i\omega s} \delta(\mathbf{x} - \mathbf{y})$$
(3)

with a boundary condition similar to (2) for \tilde{g} .

To cast (3) into a Boundary Integral Equation (BIE), we use a direct formulation procedure. ¹⁵ Consider the free space Green's function for the adjoint problem,

$$(-i\omega - \mathbf{U} \cdot \nabla)^2 \tilde{g}_0 - \nabla^2 \tilde{g}_0 = \delta(\mathbf{x} - \mathbf{z})$$
(4)

where $\tilde{g}_0(\mathbf{x}, \mathbf{z}, \omega)$ satisfies only the far field radiation condition. The solution for \tilde{g}_0 is well-known as

$$\tilde{g}_0(\mathbf{x}, \mathbf{z}, \omega) = e^{i\omega M(x_1 - z_1)/\beta^2} \frac{e^{i\frac{\omega}{\beta}\sqrt{(x_1 - z_1)^2/\beta^2 + (x_2 - z_2)^2 + (x_3 - z_3)^2}}}{4\pi\beta\sqrt{(x_1 - z_1)^2/\beta^2 + (x_2 - z_2)^2 + (x_3 - z_3)^2}}$$
(5)

where

$$\beta = \sqrt{1 - M^2}$$

By multiplying (3) with $\tilde{g}_0(\mathbf{x}, \mathbf{z}, \omega)$ and (4) with $\tilde{g}(\mathbf{x}, \mathbf{y}, \omega, s)$ and subtracting the two equations, it can be shown that

$$\nabla[-2i\omega\tilde{g}_0\tilde{g}\mathbf{U} + (\tilde{g}_0\mathbf{U}\cdot\nabla\tilde{g} - \tilde{g}\mathbf{U}\cdot\nabla\tilde{g}_0)\mathbf{U} - (\tilde{g}_0\nabla\tilde{g} - \tilde{g}\nabla\tilde{g}_0)] = \tilde{g}_0(\mathbf{x}, \mathbf{z}, \omega)e^{i\omega s}\delta(\mathbf{x} - \mathbf{y}) - \tilde{g}(\mathbf{x}, \mathbf{y}, \omega, s)\delta(\mathbf{x} - \mathbf{z})$$
(6)

By integrating the above over the body of fluids external to all solid bodies and applying the Divergence Theorem, we will get

$$e^{i\omega s}\tilde{g}_{0}(\mathbf{y},\mathbf{z},\omega) - \tilde{g}(\mathbf{z},\mathbf{y},\omega,s) = \int_{S} \mathbf{n} \cdot [-2i\omega\tilde{g}_{0}\tilde{g}\mathbf{U} + (\tilde{g}_{0}\mathbf{U} \cdot \nabla\tilde{g} - \tilde{g}\mathbf{U} \cdot \nabla\tilde{g}_{0})\mathbf{U} - (\tilde{g}_{0}\nabla\tilde{g} - \tilde{g}\nabla\tilde{g}_{0})]d\mathbf{x}_{s}$$
(7)

where S denotes all solid surfaces and \mathbf{x}_s is a point on S. In our derivation, we will assume that the normal vector \mathbf{n} is **out of** the fluid and into the solid bodies. After further simplification of (7) and an application of the solid wall boundary condition for \tilde{g} , we have the following integral relation for the exact Green's function, with the arguments of all functions given explicitly,

$$\tilde{g}(\mathbf{z}, \mathbf{y}, \omega, s) = \tilde{g}_0(\mathbf{y}, \mathbf{z}, \omega)e^{i\omega s} + \int_S \left[2i\omega U_{\mathbf{n}}\tilde{g}_0(\mathbf{x}_s, \mathbf{z}, \omega)\tilde{g}(\mathbf{x}_s, \mathbf{y}, \omega, s) + U_{\mathbf{n}}[\mathbf{U} \cdot \nabla \tilde{g}_0(\mathbf{x}_s, \mathbf{z}, \omega)]\tilde{g}(\mathbf{x}_s, \mathbf{y}, \omega, s)\right]$$

$$-\frac{\partial \tilde{g}_{0}}{\partial n}(\mathbf{x}_{s}, \mathbf{z}, \omega)\tilde{g}(\mathbf{x}_{s}, \mathbf{y}, \omega, s) - U_{\mathbf{n}}\tilde{g}_{0}(\mathbf{x}_{s}, \mathbf{z}, \omega)[\mathbf{U} \cdot \nabla \tilde{g}(\mathbf{x}_{s}, \mathbf{y}, \omega, s)]\right] d\mathbf{x}_{s}$$
(8)

where

$$U_{\mathbf{n}} \equiv \mathbf{n} \cdot \mathbf{U}$$

Equation (8) shows that $\tilde{g}(\mathbf{z}, \mathbf{y}, \omega, s)$ at any field point \mathbf{z} can be found through an integral that involves only the value of \tilde{g} on the solid surfaces, namely, $\tilde{g}(\mathbf{x}_s, \mathbf{y}, \omega, s)$. By the limit $\mathbf{z} \to \mathbf{z}_s$ where \mathbf{z}_s is a boundary point, (8) will yield a boundary integral equation for $\tilde{g}(\mathbf{x}_s, \mathbf{y}, \omega, s)$.

B. Cylindrical Bodies

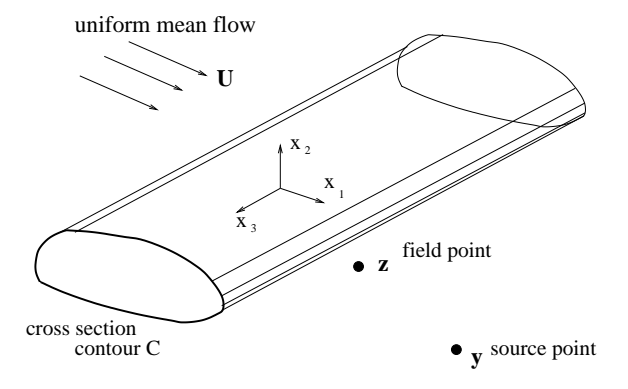


Figure 1. Schematic of a cylindrical body in a uniform flow.

We will consider a special case where all the surfaces have a constant cross section in the x_1 - x_2 plane, i.e., the equation for the solid surface is independent of a third variable x_3 , as illustrated in Figure 1. Now consider the Fourier transform of $\tilde{g}(\mathbf{z}, \mathbf{y}, \omega, s)$ in z_3 as

$$\hat{g}(\bar{\mathbf{z}}, k_3, \mathbf{y}, \omega, s) = \int_{-\infty}^{\infty} \tilde{g}(\mathbf{z}, \mathbf{y}, \omega, s) e^{ik_3 z_3} dz_3$$
(9)

and its inverse

$$\tilde{g}(\mathbf{z}, \mathbf{y}, \omega, s) = \frac{1}{2\pi} \int_{-\infty}^{\infty} \hat{g}(\bar{\mathbf{z}}, k_3, \mathbf{y}, \omega, s) e^{-ik_3 z_3} dk_3$$
(10)

where a hat denotes the transformed function and $\bar{\mathbf{z}} = (z_1, z_2)$.

By applying the Fourier transform to (8), we get

$$\hat{g}(\bar{\mathbf{z}}, k_3, \mathbf{y}, \omega, s) = \hat{g}_0(\mathbf{y}, \bar{\mathbf{z}}, k_3, \omega) e^{i\omega s} + \int_S \left[2i\omega U_{\mathbf{n}} \hat{g}_0(\mathbf{x}_s, \bar{\mathbf{z}}, k_3, \omega) \tilde{g}(\mathbf{x}_s, \mathbf{y}, \omega, s) + U_{\mathbf{n}} [\mathbf{U} \cdot \nabla \hat{g}_0(\mathbf{x}_s, \bar{\mathbf{z}}, k_3, \omega)] \tilde{g}(\mathbf{x}_s, \mathbf{y}, \omega, s) \right]$$

$$-\frac{\partial \hat{g}_0}{\partial n}(\mathbf{x}_s, \bar{\mathbf{z}}, k_3, \omega) \tilde{g}(\mathbf{x}_s, \mathbf{y}, \omega, s) - U_{\mathbf{n}} \hat{g}_0(\mathbf{x}_s, \bar{\mathbf{z}}, k_3, \omega, s) [\mathbf{U} \cdot \nabla \tilde{g}(\mathbf{x}_s, \mathbf{y}, \omega)] d\mathbf{x}_s$$
(11)

The first term in (11) is the Fourier transform of the free space Green's function $\tilde{g}_0(\mathbf{y}, \mathbf{z}, \omega)$, which is the following,

$$\hat{g}_{0}(\mathbf{y}, \bar{\mathbf{z}}, k_{3}, \omega) = \int_{-\infty}^{\infty} e^{i\omega M(y_{1}-z_{1})/\beta^{2}} \frac{e^{i\frac{\omega}{\beta}\sqrt{(y_{1}-z_{1})^{2}/\beta^{2}+(y_{2}-z_{2})^{2}+(y_{3}-z_{3})^{2}}}}{4\pi\beta\sqrt{(y_{1}-z_{1})^{2}/\beta^{2}+(y_{2}-z_{2})^{2}+(y_{3}-z_{3})^{2}}} e^{ik_{3}z_{3}} dz_{3} = e^{ik_{3}y_{3}} G_{0}(\bar{\mathbf{y}}, \bar{\mathbf{z}}, \bar{\omega})$$
(12)

where

$$G_0(\bar{\mathbf{y}}, \bar{\mathbf{z}}, \bar{\omega}) = \frac{i}{4\beta} e^{i\omega M(y_1 - z_1)/\beta^2} H_0^{(1)}(\bar{\omega}\bar{r})$$

$$\tag{13}$$

and an over bar denotes two-dimensionalized variables,

$$\bar{\mathbf{y}} = (y_1, y_2), \ \bar{r} = \sqrt{(y_1 - z_1)^2 / \beta^2 + (y_2 - z_2)^2}, \ \text{and} \ \bar{\omega} = \sqrt{\omega^2 / \beta^2 - k_3^2}$$

Further, since the surface cross section is independent of z_3 , the surface integral in (11) can now be written as follows,

$$\hat{g}(\bar{\mathbf{z}},k_3,\mathbf{y},\omega,s) = e^{ik_3y_3}e^{i\omega s}G_0(\bar{\mathbf{y}},\bar{\mathbf{z}},\bar{\omega}) + \int_C \int_{-\infty}^{\infty} \left[2i\omega U_{\mathbf{n}}e^{ik_3x_3}G_0(\bar{\mathbf{x}}_s,\bar{\mathbf{z}},\bar{\omega})\tilde{g}(\mathbf{x}_s,\mathbf{y},\omega,s) + U_{\mathbf{n}}[\mathbf{U}\cdot\nabla e^{ik_3x_3}G_0(\bar{\mathbf{x}}_s,\bar{\mathbf{z}},\bar{\omega})]\tilde{g}(\mathbf{x}_s,\mathbf{y},\omega,s) \right] \right]$$

$$-e^{ik_3x_3}\frac{\partial G_0}{\partial n}(\bar{\mathbf{x}}_s,\bar{\mathbf{z}},\bar{\omega})\tilde{g}(\mathbf{x}_s,\mathbf{y},\omega,s) - U_{\mathbf{n}}e^{ik_3x_3}G_0(\bar{\mathbf{x}}_s,\bar{\mathbf{z}},\bar{\omega})[\mathbf{U}\cdot\nabla\tilde{g}(\mathbf{x}_s,\mathbf{y},\omega)]\right]dx_3d\bar{\mathbf{x}}_s$$

where C is the contour of the surface cross section. Upon carrying out the integral for x_3 , we get an equation for $\hat{g}(\bar{\mathbf{z}}, k_3, \mathbf{y}, \omega, s)$ as

$$\hat{g}(\bar{\mathbf{z}}, k_3, \mathbf{y}, \omega, s) = e^{ik_3y_3}e^{i\omega s}G_0(\bar{\mathbf{y}}, \bar{\mathbf{z}}, \bar{\omega}) + \int_C \left[2i\omega U_{\mathbf{n}}G_0(\bar{\mathbf{x}}_s, \bar{\mathbf{z}}, \bar{\omega})\hat{g}(\bar{\mathbf{x}}_s, k_3, \mathbf{y}, \omega, s) + U_{\mathbf{n}}[\mathbf{U} \cdot \nabla G_0(\bar{\mathbf{x}}_s, \bar{\mathbf{z}}, \bar{\omega})]\hat{g}(\bar{\mathbf{x}}_s, k_3, \mathbf{y}, \omega, s) \right]$$

$$-\frac{\partial G_0}{\partial n}(\bar{\mathbf{x}}_s, \bar{\mathbf{z}}, \bar{\omega})\hat{g}(\bar{\mathbf{z}}_s, k_3, \mathbf{y}, \omega, s) - U_{\mathbf{n}}G_0(\bar{\mathbf{x}}_s, \bar{\mathbf{z}}, \bar{\omega})[\mathbf{U} \cdot \nabla \hat{g}(\bar{\mathbf{x}}_s, k_3, \mathbf{y}, \omega)]\right] d\bar{\mathbf{x}}_s$$
(14)

Finally, it is convenient to express $\hat{g}(\bar{\mathbf{z}}, k_3, \mathbf{y}, \omega, s)$ as

$$\hat{q}(\bar{\mathbf{z}}, k_3, \mathbf{y}, \omega, s) = e^{i\omega s} e^{ik_3 y_3} G_B(\bar{\mathbf{z}}, \bar{\mathbf{y}}, \bar{\omega})$$
(15)

and, after further simplifications, equation (14) can be written in terms of $G_B(\bar{\mathbf{z}}, \bar{\mathbf{y}}, \bar{\omega})$ as

$$G_B(\bar{\mathbf{z}}, \bar{\mathbf{y}}, \bar{\omega}) = e^{i\omega s} G_0(\bar{\mathbf{y}}, \bar{\mathbf{z}}, \bar{\omega}) + \int_C \left[i\omega U_{\mathbf{n}} G_0(\bar{\mathbf{x}}_s, \bar{\mathbf{z}}, \bar{\omega}) G_B(\bar{\mathbf{x}}_s, \bar{\mathbf{y}}, \bar{\omega}) - G_1(\bar{\mathbf{x}}_s, \bar{\mathbf{z}}, \bar{\omega}) G_B(\bar{\mathbf{x}}_s, \bar{\mathbf{y}}, \bar{\omega}) \right]$$

$$-U_{\mathbf{n}}U_{\mathbf{t}}G_{0}(\bar{\mathbf{x}}_{s},\bar{\mathbf{z}},\bar{\boldsymbol{\omega}})\frac{\partial G_{B}(\bar{\mathbf{x}}_{s},\bar{\mathbf{y}},\bar{\boldsymbol{\omega}})}{\partial \bar{x}_{s}}\Big]d\bar{\mathbf{x}}_{s}$$
(16)

where $G_0(\bar{\mathbf{x}}_s, \bar{\mathbf{z}}, \bar{\omega})$ is that given (13) and

$$G_1(\bar{\mathbf{x}}, \bar{\mathbf{z}}, \bar{\omega}) = -\frac{i\bar{\omega}}{4\beta} e^{i\frac{\omega M(x_1 - z_1)}{\beta^2}} \frac{(\bar{\mathbf{x}} - \bar{\mathbf{z}}) \cdot \mathbf{n}}{\bar{r}} H_1^{(1)}(\bar{\omega}\bar{r})$$
(17)

Here $\frac{\partial G_B(\bar{\mathbf{x}}_s,\bar{\mathbf{y}},\bar{\omega})}{\partial \bar{x}_s}$ in (16) is the tangential derivative of G_B on the contour C and $U_{\mathbf{t}}$ in (16) is the tangent component of the mean velocity \mathbf{U} . It is easy to show that (16) is equivalent to the integral relation for the true 2D convective Helmholtz equation with $k_3=0$, e.g., in refs[1,9].

By the limit $\bar{z} \to \bar{z}_s$ in (16) where \bar{z}_s is a point on C, we have the following boundary integral equation

$$C_sG_B(\bar{\mathbf{z}}_s, \bar{\mathbf{y}}, \bar{\omega}) = G_0(\bar{\mathbf{y}}, \bar{\mathbf{z}}_s, \bar{\omega}) + \int_C i\omega U_\mathbf{n} G_B(\bar{\mathbf{x}}_s, \bar{\mathbf{y}}, \bar{\omega}) G_0(\bar{\mathbf{x}}_s, \bar{\mathbf{z}}_s, \bar{\omega}) d\bar{\mathbf{x}}_s - \int_C G_1(\bar{\mathbf{x}}_s, \bar{\mathbf{z}}_s, \bar{\omega}) G_B(\bar{\mathbf{x}}_s, \bar{\mathbf{y}}, \bar{\omega}) d\bar{\mathbf{x}}_s$$

$$-\int_{C} U_{\mathbf{n}} U_{\mathbf{t}} \frac{\partial G_{B}(\bar{\mathbf{x}}_{s}, \bar{\mathbf{y}}, \bar{\omega})}{\partial \bar{x}_{s}} G_{0}(\bar{\mathbf{x}}_{s}, \bar{\mathbf{z}}_{s}, \bar{\omega}) d\bar{\mathbf{x}}_{s}$$
(18)

In the above, C_s is a constant resulted from the singular kernel $G_1(\bar{\mathbf{x}}_s, \bar{\mathbf{z}}_s, \bar{\omega})$ in the limit process. Its value in general depends on the smoothness of the boundary. For two-dimensional boundaries, the value for C_s is given explicitly in ref[9]. On a smooth boundary point, the value of C_s has been found to be $\frac{1}{2}$, independent of the mean flow Mach number. In the spectral collocation method to be discussed below, the collocation points are the interior Gauss-Chebyshev points and thus will always be smooth boundary points.

III. Spectral collocation Boundary Element Method

We will use a spectral collocation boundary element method to solve the boundary integral equation (18). Let the boundary C be discretized into elements Γ_j as

$$C = \bigcup_{j=1}^{N} \Gamma_j$$

On each element Γ_j , let the boundary be parametrized as

$$\bar{\mathbf{x}}_s = \mathbf{r}_i(t), t \in [0, 1] \tag{19}$$

where t is the local parameterization variable and $\mathbf{r}_j(t)$ is a cubic spline connecting grid points on the boundary with continuous tangential derivatives on smooth boundaries. The solution $G_B(\bar{\mathbf{x}}_s, \bar{\mathbf{y}}, \bar{\omega})$ on each Γ_j as a function of t is approximated by an expansion in a set of basis functions $\{\phi_n(t), n=0,1,2,...,P\}$ as

$$G_B(\bar{\mathbf{x}}_s, \bar{\mathbf{y}}, \bar{\omega}) = G_B(\mathbf{r}_j(t), \bar{\mathbf{y}}, \bar{\omega}) = \sum_{n=0}^P u_j^{(n)} \phi_n(t)$$
(20)

where $u_j^{(n)}$ are the expansion coefficients and P is the highest order of the polynomials in the expansion. By substituting (20) into the right hand side of (18), we get

$$\frac{1}{2}G_B(\bar{\mathbf{z}}_s, \bar{\mathbf{y}}, \bar{\omega}) = G_0(\bar{\mathbf{y}}, \bar{\mathbf{z}}_s, \bar{\omega}) - \sum_{j=1}^N \int_0^1 G_1(\mathbf{r}_j(t), \bar{\mathbf{z}}_s, \bar{\omega}) \left[\sum_{n=0}^P u_j^{(n)} \phi_n(t) \right] |\mathbf{r}_j'(t)| dt$$

$$+\sum_{j=1}^{N}\int_{0}^{1}i\omega U_{\mathbf{n}}G_{0}(\mathbf{r}_{j}(t),\bar{\mathbf{z}}_{s},\bar{\omega})\left[\sum_{n=0}^{P}u_{j}^{(n)}\phi_{n}(t)\right]\left|\mathbf{r}_{j}'(t)\right|dt - \sum_{j=1}^{N}\int_{0}^{1}U_{\mathbf{n}}U_{\mathbf{t}}G_{0}(\mathbf{r}_{j}(t),\bar{\mathbf{z}}_{s},\bar{\omega})\left[\sum_{n=0}^{P}u_{j}^{(n)}\phi_{n}'(t)\right]dt$$

$$(21)$$

where a prime indicates the derivative with respect to t. (Note that for the tangential derivative of G_B appeared in the last term of (18), we have

$$\frac{\partial G_B(\bar{\mathbf{x}}_s, \bar{\mathbf{y}}, \bar{\omega})}{\partial \bar{x}_s} = \nabla G_B \cdot \frac{\mathbf{r}'(t)}{|\mathbf{r}'(t)|} = \frac{1}{|\mathbf{r}'(t)|} \frac{\partial G_B}{\partial t} \Big)$$

In the spectral collocation method, we force (21) to be satisfied on a set of collocation points (Appendix)

$$\bar{\mathbf{z}}_s = \bar{\mathbf{z}}_i^{(\ell)}$$
 on element Γ_i where $\bar{\mathbf{z}}_i^{(\ell)} = \mathbf{r}_i(t_\ell), \ell = 0, 1, ..., P$

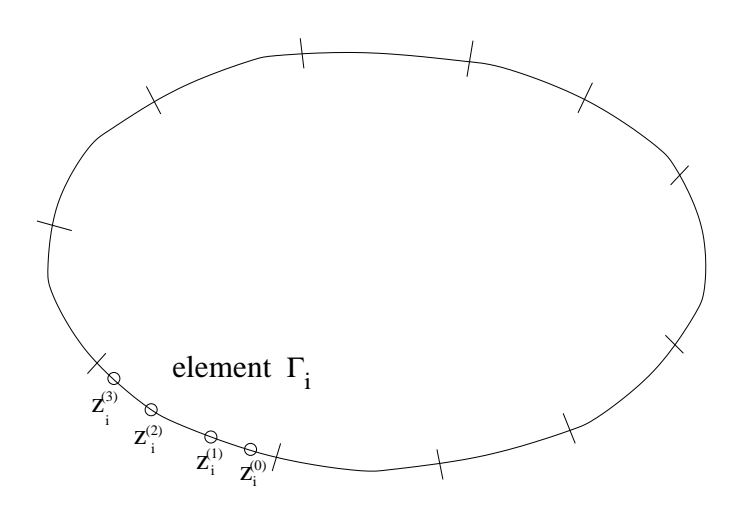


Figure 2. Schematic diagram showing boundary elements and collocation points.

This yields immediately the following linear system of equations for the expansion coefficients,

$$\frac{1}{2} \sum_{n=0}^{P} u_i^{(n)} \phi_n(t_\ell) = G_0(\bar{\mathbf{y}}, \bar{\mathbf{z}}_i^{(\ell)}, \bar{\omega}) - \sum_{j=1}^{N} \int_0^1 G_1(\mathbf{r}_j(t), \bar{\mathbf{z}}_i^{(\ell)}, \bar{\omega}) \left[\sum_{n=0}^{P} u_j^{(n)} \phi_n(t) \right] |\mathbf{r}_j'(t)| dt$$

$$+\sum_{j=1}^{N}\int_{0}^{1}i\omega U_{\mathbf{n}}G_{0}(\mathbf{r}_{j}(t),\bar{\mathbf{z}}_{i}^{(\ell)},\bar{\omega})\left[\sum_{n=0}^{P}u_{j}^{(n)}\phi_{n}(t)\right]\left|\mathbf{r}_{j}^{\prime}(t)\right|dt -\sum_{j=1}^{N}\int_{0}^{1}U_{\mathbf{n}}U_{\mathbf{t}}G_{0}(\mathbf{r}_{j}(t),\bar{\mathbf{z}}_{i}^{(\ell)},\bar{\omega})\left[\sum_{n=0}^{P}u_{j}^{(n)}\phi_{n}^{\prime}(t)\right]dt$$
(22)

for $\ell=0,1,..,P, i=1,...,N.$ The system of equations (22) can be written as

$$\mathbf{H}\mathbf{u} = \mathbf{g} \tag{23}$$

where **u** is a vector that contains all the expansion coefficients $u_i^{(n)}$,

$$\mathbf{u} = \begin{bmatrix} u_1^{(0)} \\ u_1^{(1)} \\ \vdots \\ u_N^{(P)} \end{bmatrix}_{N(P+1) \times 1}$$

The entries for matrix H and g are

$$\left\{\mathbf{H}\right\}_{IJ} = \frac{1}{2}\phi_n(t_\ell)\delta_{ij} + \int_0^1 G_1(\mathbf{r}_j(t), \bar{\mathbf{z}}_i^{(\ell)}, \bar{\omega})\phi_n(t) \left|\mathbf{r}_j'(t)\right| dt - \int_0^1 i\omega U_{\mathbf{n}}G_0(\mathbf{r}_j(t), \bar{\mathbf{z}}_i^{(\ell)}, \bar{\omega})\phi_n(t) \left|\mathbf{r}_j'(t)\right| dt$$

$$+ \int_0^1 U_{\mathbf{n}} U_{\mathbf{t}} G_0(\mathbf{r}_j(t), \bar{\mathbf{z}}_i^{(\ell)}, \bar{\omega}) \phi_n'(t) dt$$
 (24)

$$\{\mathbf{g}\}_{t} = G_{0}(\bar{\mathbf{y}}, \bar{\mathbf{z}}_{i}^{(\ell)}, \bar{\omega}) \tag{25}$$

with
$$I = (i-1)(P+1) + \ell$$
 and $J = (j-1)(P+1) + n$, for $\ell, n = 0, 1, 2, ..., P$.

For results reported in this paper, Chebyshev polynomials will be used as the basis functions and the interior Gauss-Chebyshev points as collocation points (Appendix). To achieve spectral accuracy, it is important to treat properly the singularities present in the integrals in forming the \mathbf{H} matrix from (24). When the collocation point is on the element of integration, i.e., when j=i, the kernel functions $G_0(\mathbf{r}_i(t),\bar{\mathbf{z}}_i^{(\ell)},\bar{\omega})$ and $G_1(\mathbf{r}_i(t),\bar{\mathbf{z}}_i^{(\ell)},\bar{\omega})$ in (24) will have a logarithmic singularity. Specifically, recall that by (13), we have

$$G_0(\mathbf{r}_i(t), \bar{\mathbf{z}}_i^{(\ell)}, \bar{\omega}) = \frac{iE}{4\beta} H_0^{(1)}(\bar{\omega}\bar{r})$$
(26)

in which $E=e^{i\omega M[\mathbf{r}_i(t)-\mathbf{\bar{z}}_i^{(\ell)}]_1/\beta^2}$ and

$$\bar{r} = \sqrt{[\mathbf{r}_i(t) - \bar{\mathbf{z}}_i^{(\ell)}]_1^2 / \beta^2 + [\mathbf{r}_i(t) - \bar{\mathbf{z}}_i^{(\ell)}]_2^2} = \sqrt{[\mathbf{r}_i(t) - \mathbf{r}_i(t_\ell)]_1^2 / \beta^2 + [\mathbf{r}_i(t) - \mathbf{r}_i(t_\ell)]_2^2}$$

$$\approx |t - t_{\ell}| \sqrt{[\mathbf{r}_{\ell}'(t_{\ell})]_{1}^{2}/\beta^{2} + [\mathbf{r}_{\ell}'(t_{\ell})]_{2}^{2}}$$
(27)

In the above, $[\cdot]_1$ and $[\cdot]_2$ denote the first and second components of the vector in the brackets. For Hankel function of the first kind $H_0^{(1)}(z)$, we have

$$H_0^{(1)}(z) = J_0(z) + iY_0(z) = \frac{2i}{\pi} \ln(z) J_0(z) + \text{smooth terms}$$
 (28)

where "smooth terms" denotes analytic and infinitely differentiable functions. This will result in a logarithmic singularity for G_0 at $t=t_\ell$ as given in (26). To separate the singular and smooth parts in $G_0(\mathbf{r}_i(t), \bar{\mathbf{z}}_i^{(\ell)}, \bar{\omega})$, following ref[8], we rewrite it as

$$G_0(\mathbf{r}_i(t), \bar{\mathbf{z}}_i^{(\ell)}, \bar{\omega}) = \frac{iE}{4\beta} \left[H_0^{(1)}(\bar{\omega}\bar{r}) - \frac{2i}{\pi} \ln(|t - t_\ell|) J_0(\bar{\omega}\bar{r}) \right] + \frac{iE}{4\beta} \frac{2i}{\pi} \ln(|t - t_\ell|) J_0(\bar{\omega}\bar{r})$$

$$\equiv G_0^{(\mathbf{A})}(\mathbf{r}_j(t), \bar{\mathbf{z}}_i^{(\ell)}, \bar{\omega}) + G_0^{(\mathbf{B})}(\mathbf{r}_j(t), \bar{\mathbf{z}}_i^{(\ell)}, \bar{\omega}) \ln|t - t_\ell|$$

Then, an integral involving G_0 on a singular element, when j = i, will be carried out as follows,

$$\int_{0}^{1} \Psi(t) G_{0}(\mathbf{r}_{i}(t), \bar{\mathbf{z}}_{i}^{(\ell)}, \bar{\omega}) dt = \int_{0}^{1} \Psi(t) G_{0}^{(\mathbf{A})}(\mathbf{r}_{i}(t), \bar{\mathbf{z}}_{i}^{(\ell)}, \bar{\omega}) dt + \int_{0}^{1} \Psi(t) G_{0}^{(\mathbf{B})}(\mathbf{r}_{i}(t), \bar{\mathbf{z}}_{i}^{(\ell)}, \bar{\omega}) \ln|t - t_{\ell}| dt \quad (29)$$

where the first integral is evaluated by a regular Gauss-Legendre quadrature and the second integral is to be evaluated using a logarithmic quadrature.

Similarly, it can be shown that $G_1(\mathbf{r}_i(t), \bar{\mathbf{z}}_i^{(\ell)}, \bar{\omega})$ as defined in (17) has also a logarithmic singularity at $t=t_\ell$, see ref[8], even though $G_1(\mathbf{r}_i(t), \bar{\mathbf{z}}_i^{(\ell)}, \bar{\omega})$ actually remains finite. To accurately evaluate the integral, by the asymptotic expansion of $H_1(z)$, we again rewrite $G_1(\mathbf{r}_i(t), \bar{\mathbf{z}}_i^{(\ell)}, \bar{\omega})$ as

$$G_{1}(\mathbf{r}_{i}(t), \bar{\mathbf{z}}_{i}^{(\ell)}, \bar{\omega}) = \frac{i\bar{\omega}F}{4\beta} [H_{1}^{(1)}(\bar{\omega}\bar{r}) - \frac{2i}{\pi} \ln(|t - t_{\ell}|) J_{1}(\bar{\omega}\bar{r})] - \frac{i\bar{\omega}F}{4\beta} \frac{2i}{\pi} \ln(|t - t_{\ell}|) J_{1}(\bar{\omega}\bar{r})$$

$$\equiv G_{1}^{(\mathbf{A})}(\mathbf{r}_{i}(t), \bar{\mathbf{z}}_{i}^{(\ell)}, \bar{\omega}) + G_{1}^{(\mathbf{B})}(\mathbf{r}_{i}(t), \bar{\mathbf{z}}_{i}^{(\ell)}, \bar{\omega}) \ln|t - t_{\ell}|$$

where $F = E[(\mathbf{r}_i - \bar{\mathbf{z}}_i^{(\ell)}) \cdot \mathbf{n}]/\bar{r}$ by the definition in (17). Then, the integral involving $G_1(\mathbf{r}_i(t), \bar{\mathbf{z}}_i^{(\ell)}, \bar{\omega})$ in (24) is carried out in a similar manner as in (29).

Once **u** is found, $G_B(\bar{\mathbf{z}}, \bar{\mathbf{y}}, \bar{\omega})$ can be computed by (16) and the 3D Green's function $\tilde{g}(\mathbf{z}, \mathbf{y}, \omega, s)$ by (10). Further computational details are given in the next section.

IV. Numerical solutions

A. Two-dimensional (2D) solutions

We will first show examples of the spectral collocation method in 2D cases, i.e., the numerical solutions of (18) with $k_3 = 0$.

After the expansion coefficients $u_j^{(n)}$ are found from the linear system (23), the value of the Green's function at any field point $\bar{\mathbf{z}} = (z_1, z_2)$ is computed as the following, with all the arguments given explicitly,

$$G_B(\bar{\mathbf{z}}, \bar{\mathbf{y}}, \bar{\omega}) = G_0(\bar{\mathbf{y}}, \bar{\mathbf{z}}, \bar{\omega}) - \sum_{j=1}^N \int_0^1 G_1(\mathbf{r}_j(t), \bar{\mathbf{z}}, \bar{\omega}) \left[\sum_{n=0}^P u_j^{(n)} \phi_n(t) \right] \left| \mathbf{r}_j'(t) \right| dt$$

$$+\sum_{j=1}^{N}\int_{0}^{1}i\omega U_{\mathbf{n}}G_{0}(\mathbf{r}_{j}(t),\bar{\mathbf{z}},\bar{\omega})\left[\sum_{n=0}^{P}u_{j}^{(n)}\phi_{n}(t)\right]\left|\mathbf{r}_{j}'(t)\right|dt-\sum_{j=1}^{N}\int_{0}^{1}U_{\mathbf{n}}U_{\mathbf{t}}G_{0}(\mathbf{r}_{j}(t),\bar{\mathbf{z}},\bar{\omega})\left[\sum_{n=0}^{P}u_{j}^{(n)}\phi_{n}'(t)\right]dt$$
(30)

where $G_1(\mathbf{r}_0(t), \bar{\mathbf{z}}, \bar{\omega})$ and $G_1(\mathbf{r}_j(t), \bar{\mathbf{z}}, \bar{\omega})$ are known functions, defined in (13) and (17) respectively. The double divergence of the Green's function is found by taking directly the spatial derivatives of (30) as follows,

$$\frac{\partial^2}{\partial z_i \partial z_j} G_B(\bar{\mathbf{z}}, \bar{\mathbf{y}}, \bar{\omega}) = \frac{\partial^2}{\partial z_i \partial z_j} G_0(\bar{\mathbf{y}}, \bar{\mathbf{z}}, \bar{\omega}) - \sum_{j=1}^N \int_0^1 \frac{\partial^2}{\partial z_i \partial z_j} G_1(\mathbf{r}_j(t), \bar{\mathbf{z}}, \bar{\omega}) \left[\sum_{n=0}^P u_j^{(n)} \phi_n(t) \right] \left| \mathbf{r}_j'(t) \right| dt$$

$$+\sum_{j=1}^{N}\int_{0}^{1}i\omega U_{\mathbf{n}}\frac{\partial^{2}}{\partial z_{i}\partial z_{j}}G_{0}(\mathbf{r}_{j}(t),\bar{\mathbf{z}},\bar{\omega})\left[\sum_{n=0}^{P}u_{j}^{(n)}\phi_{n}(t)\right]\left|\mathbf{r}_{j}^{\prime}(t)\right|dt-\sum_{j=1}^{N}\int_{0}^{1}U_{\mathbf{n}}U_{\mathbf{t}}\frac{\partial^{2}}{\partial z_{i}\partial z_{j}}G_{0}(\mathbf{r}_{j}(t),\bar{\mathbf{z}},\bar{\omega})\left[\sum_{n=0}^{P}u_{j}^{(n)}\phi_{n}^{\prime}(t)\right]dt$$
(31)

Since the field point \bar{z} is off the boundary, all integrals in (31) are theoretically well-defined and can in principle be evaluated accurately using Gauss quadratures.

One, however, has to be careful when the field point $\bar{\mathbf{z}}$ is very close to the boundary. In such cases, the double divergence of the integral kernels in (31), $\frac{\partial^2}{\partial z_i \partial z_j} G_0(\mathbf{r}_j(t), \bar{\mathbf{z}}, \bar{\omega})$ and $\frac{\partial^2}{\partial z_i \partial z_j} G_1(\mathbf{r}_j(t), \bar{\mathbf{z}}, \bar{\omega})$, will be nearly singular on the element close to the field point $\bar{\mathbf{z}}$. This has two consequences. First, to ensure the accuracy of evaluating the integrals in (31), the integration interval [0,1] for the element nearest to the field point is refined into sub-intervals clustered around the point on the boundary that has the minimum distance to the field point $\bar{\mathbf{z}}$. Then, the integrals for

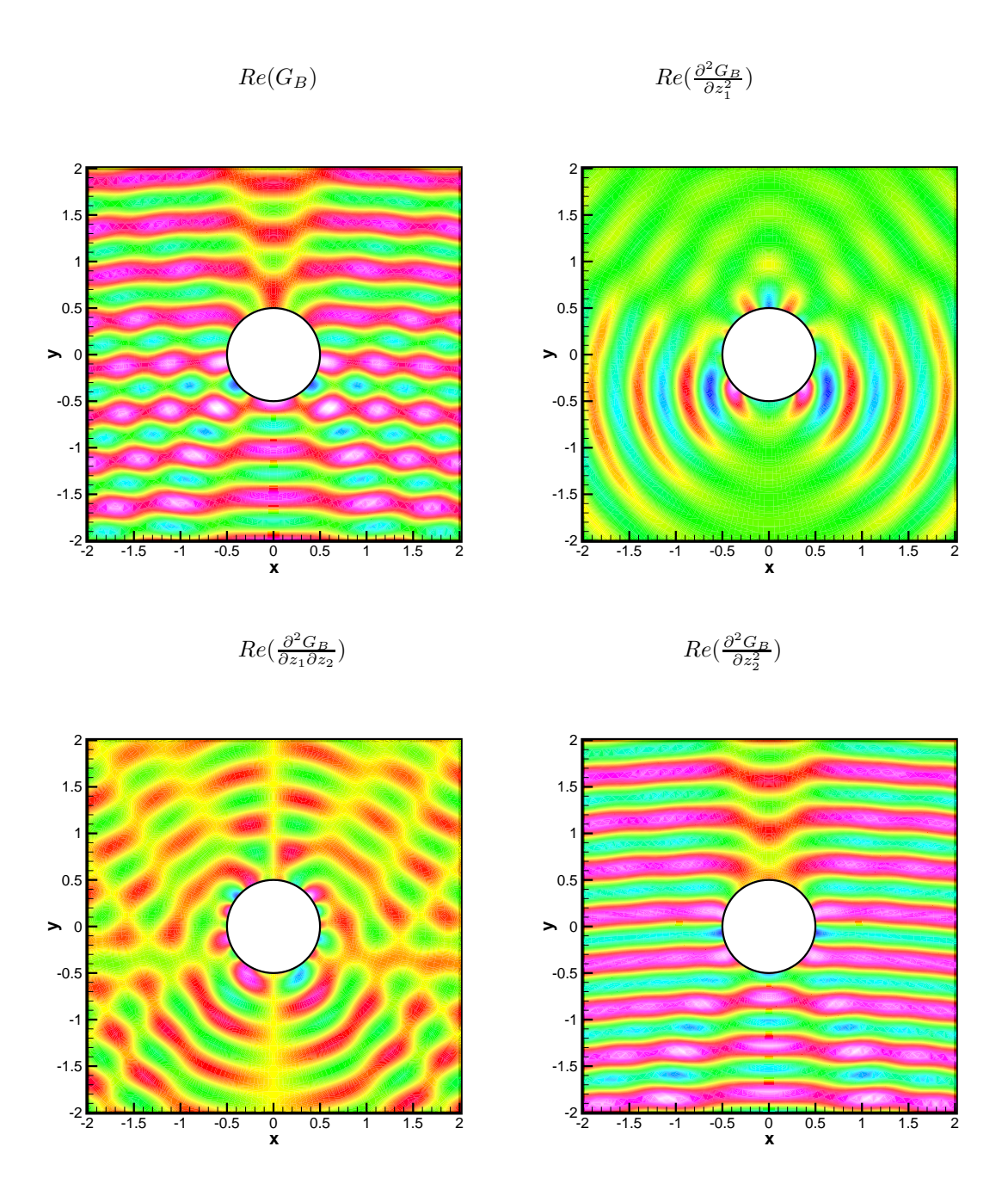


Figure 3. Contour plots of computed Green's function and its second order spatial derivatives. $\omega=4\pi,N=16$.

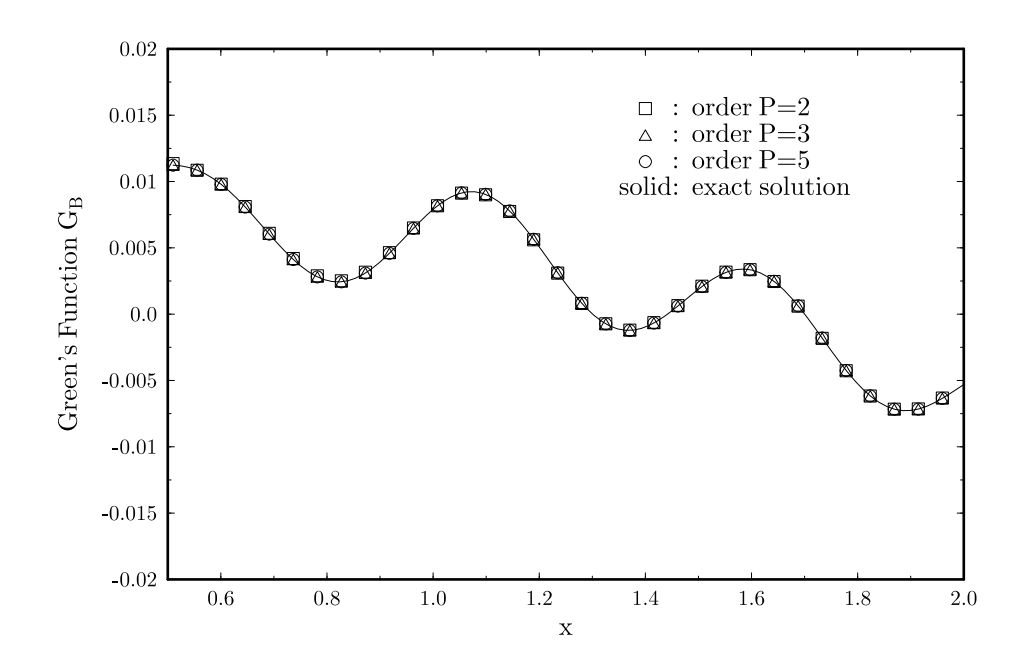


Figure 4. The computed Green's function along line $x_2=0$. The order of basis polynomials used is as indicated. Solid line is the exact solution. $\omega=4\pi, N=16$.

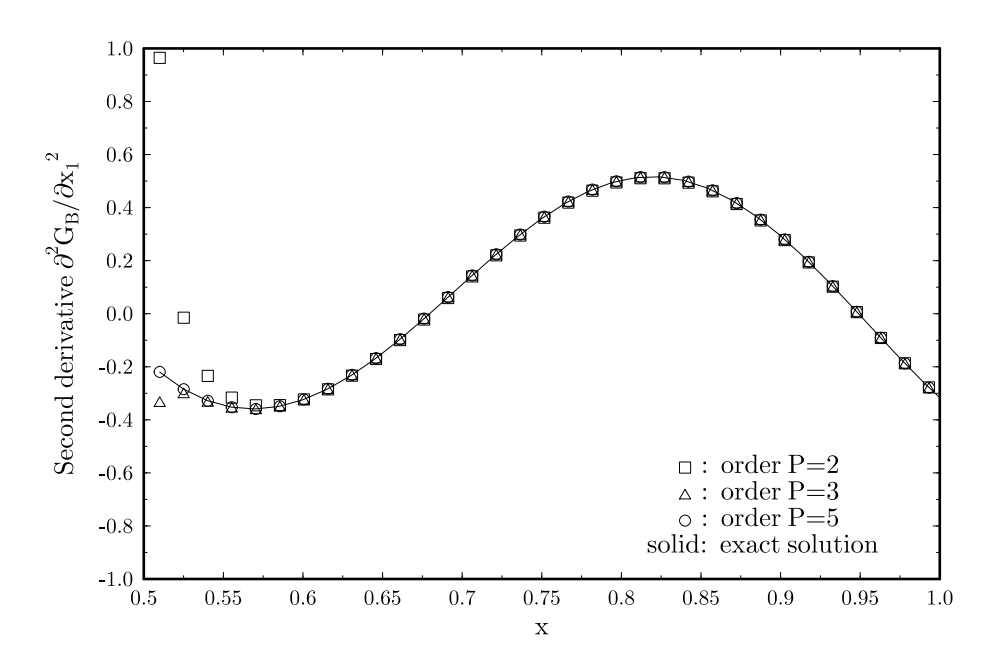


Figure 5. The computed second derivative of Green's function with respect to x_1 along line $x_2=0$. The order of basis polynomials used is as indicated. Solid line is the exact solution. $\omega=4\pi$, N=16.

each sub-interval is evaluated by a 20-point Gauss quadrature. Second, when the integral kernels in (31) are nearly singular, any numerical error in the solution of $u_j^{(n)}$ will be magnified by the kernel. As a result, better accuracy on the BEM solution is required than that for the Green's function itself, as we will illustrate further next.

In Figure 3, the contour plots of the Green's function and its double divergence for a circular cylinder of radius 0.5 are shown. The source point for this calculation is located at $\bar{y}=(0,-20)$ and the frequency $\omega=4\pi$. For this example, 16 elements are used on the cylinder. Comparison with the exact solution along $x_2=0$ is shown in Figures 4 and 5, of numerical results obtained with basis polynomials of order P=2, 3 and 5. For the values of the Green's function in Figure 4, excellent agreements are found in all three calculations. For the second derivative of the Green's function in Figure 5, however, the agreements are good for all the points except those close to the boundary at x=0.5 when the order P=2 and 3. This shows that to compute the second derivatives at field points close to the boundary, more accurate boundary element solutions than what are sufficient for the Green's function itself are necessary. Since the spectral collocation method can easily increase the order of approximation, it is well-suited for this purpose.

To demonstrate spectral accuracy of the collocation method, we show the decaying of the numerical errors at two sample field points as the order of the basis polynomials is increased. The first point (A) is at $\mathbf{z}=(0.51,0)$, very close to the boundary, and the second point (B) is at $\mathbf{z}=(0.75,0)$. Tables 1 shows the relative errors for the Green's function G_B and its second derivative $\frac{\partial^2 G_B}{\partial x_1^2}$ with Mach number M=0 and M=0.2 respectively. For the case of M=0.2, the numerical solution was compared with the values obtained using a much higher order of the basis functions (P=20). The data for Table 1 are also plotted in Figure 6. We see that as the order of the basis polynomials increases, exponential rate of decaying of the error is observed. We also see that for point A, close to the cylinder, the second derivative of the Green's function shows an error larger than that of the Green's function. This is due to the near singular behavior of the integral kernels as discussed previously.

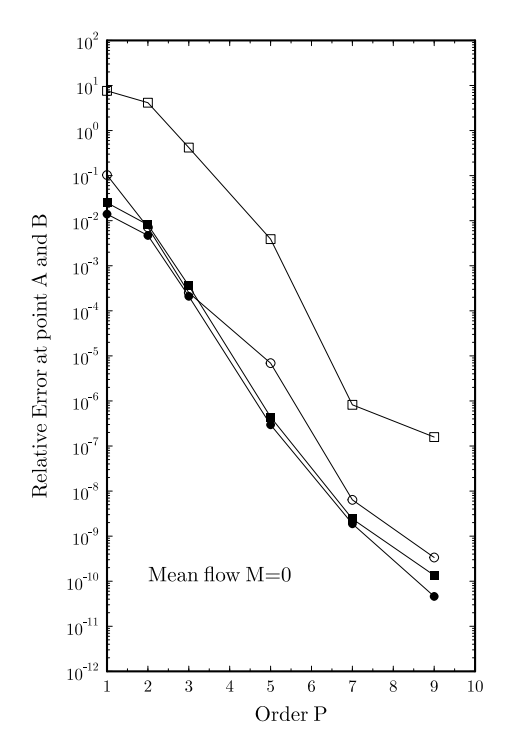
(a) $M = 0$				
Order	Point A	$\bar{\mathbf{z}} = (0.51, 0)$	Point B	$\bar{\mathbf{z}} = (0.75, 0)$
P	G_B	$rac{\partial^2 G_B}{\partial x_1^2}$	G_B	$rac{\partial^2 G_B}{\partial x_1^2}$
1	0.1038886239	7.603432629	0.01406251098	0.02500180801
2	0.007133658417	4.152256752	0.004734834074	0.008134659324
3	0.0002528658918	0.4196262382	0.0002109935459	0.0003695661646
5	$6.91008971 \times 10^{-6}$	0.003938548894	$2.962834071 \times 10^{-7}$	$4.406201266 \times 10^{-7}$
7	$6.371851995 \times 10^{-9}$	$8.215799946 \times 10^{-7}$	$1.883536454 \times 10^{-9}$	$2.417209797 \times 10^{-9}$
9	$3.369739287 \times 10^{-10}$	$1.586442069 \times 10^{-7}$	$4.653065184 \times 10^{-11}$	$1.352390864 \times 10^{-10}$

(b) $M = 0.2$						
Order	Point A	$\bar{\mathbf{z}} = (0.51, 0)$	Point B	$\bar{\mathbf{z}} = (0.75, 0)$		
P	G_B	$rac{\partial^2 G_B}{\partial x_1^2}$	G_B	$rac{\partial^2 G_B}{\partial x_1^2}$		
1	0.1521241197	9.476813276	0.04833708689	0.09978817813		
2	0.001772183931	5.013024225	0.01375715913	0.01511443759		
3	0.0003319125013	0.5012060291	0.0006810750366	0.0007443177948		
5	$4.631392271 \times 10^{-6}$	0.005235725259	$4.390344602 \times 10^{-6}$	$5.546163906 \times 10^{-6}$		
7	$1.225071762 \times 10^{-8}$	$1.250007101 \times 10^{-5}$	$6.626610248 \times 10^{-8}$	$8.564798501 \times 10^{-8}$		
9	$6.328697464 \times 10^{-10}$	$8.757772821 \times 10^{-8}$	$8.681963092 \times 10^{-10}$	$1.224935822 \times 10^{-9}$		

Table 1. Relative errors of computed Green's function and its second derivative with respect to x_1 as the order of the basis polynomial P increases. In all calculations, the number of elements on the cylinder N=16. The mean flow Mach number is (a) M=0; (b) M=0.2.

B. Three-dimensional (3D) point source

The Green's function of a 3D point source will be constructed using the 2D solutions discussed above by the Fourier inverse integral given in (10). In carrying out the integral in k_3 , we will include only the "propagating" modes of the 2D solutions, namely, for $|k_3| \le \omega/\beta$. Recalling (15), this gives



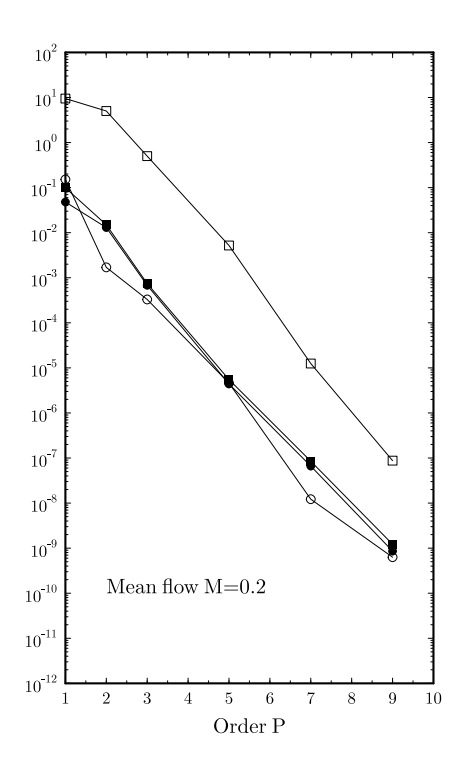


Figure 6. Relative error as a function of the order of basis polynomials. Open symbol: at point A; Filled symbol: at point B; Circles: G_B ; Squares: $\frac{\partial^2 G_B}{\partial x_1^2}$.

$$\tilde{g}(\mathbf{z}, \mathbf{y}, \omega, s) = \frac{1}{2\pi} \int_{-\omega/\beta}^{\omega/\beta} e^{i\omega s} e^{ik_3 y_3} G_B(\bar{\mathbf{z}}, \bar{\mathbf{y}}, \bar{\omega}) e^{-ik_3 z_3} dk_3$$

$$= \frac{e^{i\omega s}}{\pi} \int_0^{\omega/\beta} G_B(\bar{\mathbf{y}}, \bar{\mathbf{z}}, \bar{\omega}) \cos[k_3 (z_3 - y_3)] dk_3$$
(32)

where $G_B(\bar{\mathbf{z}}, \bar{\mathbf{y}}, \bar{\omega})$ is the 2D solution presented in the previous section with frequency $\bar{\omega} = \sqrt{\omega^2/\beta^2 - k_3^2}$.

To evaluate the integral in (32), we note that $G_B(\bar{\mathbf{y}}, \bar{\mathbf{z}}, \bar{\omega})$ varies rapidly as $k_3 \to \omega/\beta$. To ensure accuracy, instead of using a simple trapezoid rule, ¹⁴ we use high order Gauss quadratures. The interval $[0, \omega/\beta]$ is divided into sub-intervals, i.e., $[0, \omega/\beta] = \bigcup_{i=1}^{I} [\gamma_i, \gamma_{i+1}]$, and each sub-interval is evaluated by a Gauss quadrature formula. More specifically, (32) is evaluated numerically as follows,

$$\tilde{g}(\mathbf{z}, \mathbf{y}, \omega, s) = \frac{e^{i\omega s}}{\pi} \sum_{i=1}^{I} \int_{\gamma_i}^{\gamma_{i+1}} G_B(\bar{\mathbf{y}}, \bar{\mathbf{z}}, \bar{\omega}) \cos[k_3(z_3 - y_3)] dk_3 = \frac{e^{i\omega s}}{\pi} \sum_{i=1}^{I} \sum_{j=1}^{J} w_j^{(i)} G_B(\bar{\mathbf{y}}, \bar{\mathbf{z}}, \bar{\omega}_j) \cos[\zeta_j^{(i)}(z_3 - y_3)]$$
where $\zeta_j^{(i)}$ and $w_j^{(i)}$ are the abscissas and weights of the quadrature for interval $[\gamma_i, \gamma_{i+1}]$ and $\bar{\omega}_j = \sqrt{\omega^2/\beta^2 - \zeta_j^{(i)}}^2$.

We will show the calculation of a point source with a circular cylinder where the exact solution is known.⁴ The cylinder has a radius of 0.5 and the point source is located at $\mathbf{y} = (0, -20, 0)$. The frequency is $\omega = 4\pi$. Figure 7 shows the contours slices of the computed Green's function. For this calculation, I = 20 and J = 32. The comparison with the exact solution along a line parallel to the cylinder is shown in Figure 8. The agreement is excellent.

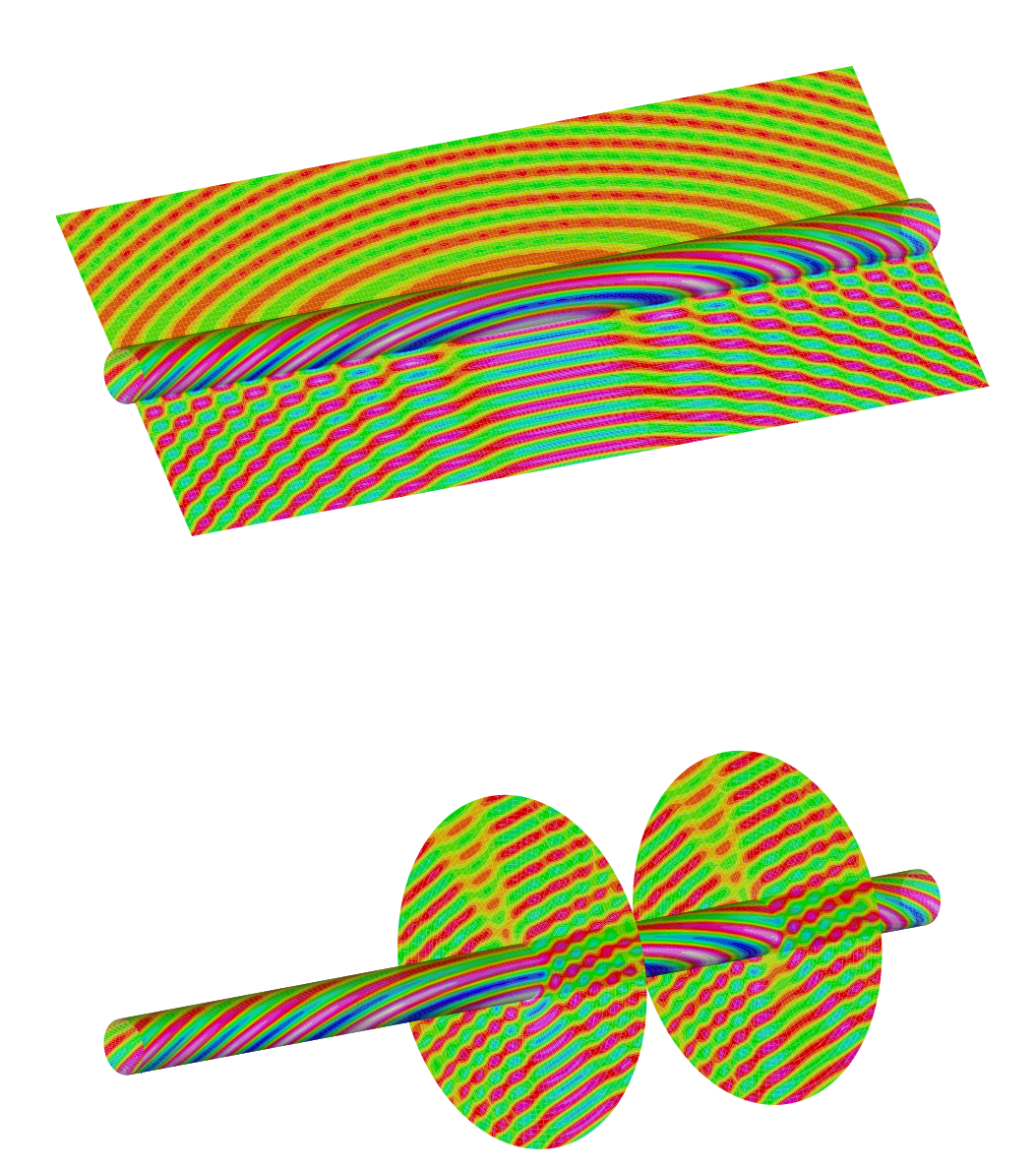


Figure 7. Contour slices of computed Green's function for a point source with a circular cylinder. Top: $z_2 - z_3$ slice at $z_1 = 0$; Bottom: $z_1 - z_2$ slices at $z_3 = 0$ and $z_$

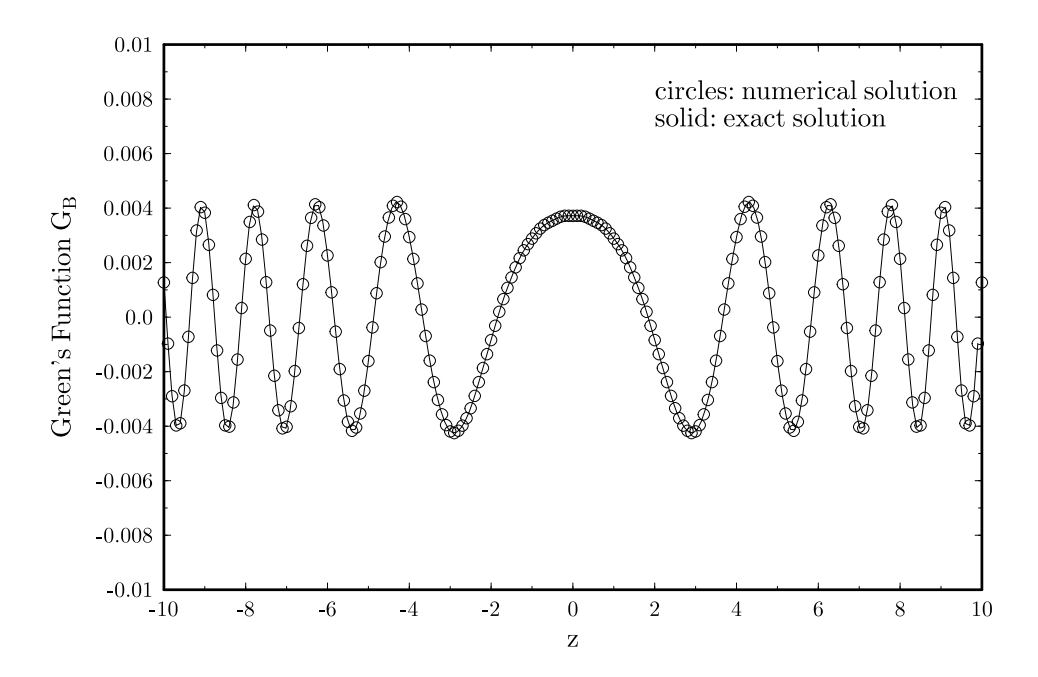


Figure 8. Comparison with the exact solution along points in z_3 direction, parallel to the cylinder, with fixed $(z_1, z_2) = (0, -0.75)$. The source point is at y = (0, -20, 0).

C. Far field approximation

The computation of Green's function $\tilde{g}(\mathbf{z}, \mathbf{y}, \omega, s)$ for the three-dimensional point source can be considerably simplified when the source point \mathbf{y} is located at the far field away from the surface and unsteady flows, as in the case when \mathbf{y} denotes the microphone location in the application of the Green's function in the acoustic analogy. Assuming $|\mathbf{y}| >> |\mathbf{z}|$, we have

$$\sqrt{(y_1 - z_1)^2/\beta^2 + (y_2 - z_2)^2 + (y_3 - z_3)^2} \approx ||\mathbf{y}|| - \hat{y}_1 z_1/\beta - \hat{y}_2 z_2 - \hat{y}_3 z_3 \tag{34}$$

where

$$||\mathbf{y}|| = \sqrt{y_1^2/\beta^2 + y_2^2 + y_3^2}, \ \hat{y}_1 = \frac{y_1}{\beta||\mathbf{y}||}, \ \hat{y}_2 = \frac{y_2}{||\mathbf{y}||}, \ \hat{y}_3 = \frac{y_3}{||\mathbf{y}||} \ \text{and} \ \hat{y}_1 + \hat{y}_2 + \hat{y}_3 = 1$$

Consequently, we have the far field approximation of the free space Green's function (5) as

$$\tilde{g}_{0}(\mathbf{y}, \mathbf{z}, \omega) \approx e^{i\frac{\omega M||\mathbf{y}||\hat{y}_{1}}{\beta} - i\frac{\omega Mz_{1}}{\beta^{2}}} \frac{e^{i\frac{\omega}{\beta}(||\mathbf{y}|| - \hat{y}_{1}z_{1}/\beta - \hat{y}_{2}z_{2} - \hat{y}_{3}z_{3})}}{4\pi\beta||\mathbf{y}||} = \frac{e^{i\frac{\omega}{\beta}||\mathbf{y}||[1+M\hat{y}_{1}]}}{4\pi\beta||\mathbf{y}||} e^{-i\frac{\omega}{\beta^{2}}[\hat{y}_{1}+M]z_{1} - i\frac{\omega}{\beta}\hat{y}_{2}z_{2} - i\frac{\omega}{\beta}\hat{y}_{3}z_{3}}}$$
(35)

and its Fourier transform in z_3 as

$$\hat{g}_0(\mathbf{x}, \bar{\mathbf{z}}, k_3, \omega) = \int_{-\infty}^{\infty} \tilde{g}_0(\mathbf{x}, \mathbf{z}, \omega) e^{ik_3 z_3} dz_3 \approx F_0(\mathbf{y}, \bar{\mathbf{z}}, \omega) \delta(k_3 - \frac{\omega}{\beta} \hat{y}_3)$$
(36)

where

$$F_0(\mathbf{y}, \bar{\mathbf{z}}, \omega) = \frac{e^{i\frac{\omega}{\beta}||\mathbf{y}||[1+M\hat{y}_1]}}{2\beta||\mathbf{y}||} e^{-i\frac{\omega}{\beta^2}[\hat{y}_1+M]z_1 - i\frac{\omega}{\beta}\hat{y}_2 z_2}$$
(37)

Therefore, by applying (36) to the first term in (11), we can assume the Fourier transform of the Green's function for $|\mathbf{y}| >> |\mathbf{z}|$ to be of the form

$$\hat{g}(\bar{\mathbf{z}}, k_3, \mathbf{y}, \omega, s) \approx e^{i\omega s} \delta(k_3 - \frac{\omega}{\beta} \hat{y}_3) G_B(\bar{\mathbf{z}}, \bar{\mathbf{y}}, \bar{\omega})$$
(38)

where $G_B(\bar{\mathbf{z}}, \bar{\mathbf{y}}, \bar{\omega})$ is the 2D boundary element solution of (18) when the first term on the right hand side of (18), $G_0(\bar{\mathbf{y}}, \bar{\mathbf{z}}, \bar{\omega})$, is replaced by $F_0(\mathbf{y}, \bar{\mathbf{z}}, \omega)$ given in (37). This gives the Green's function for the far field approximation as follows,

$$\tilde{g}(\mathbf{z}, \mathbf{y}, \omega, s) = \frac{1}{2\pi} \int_{-\infty}^{\infty} \hat{g}(\bar{\mathbf{z}}, k_3, \mathbf{y}, \omega, s) e^{-ik_3 z_3} dk_3 \approx \frac{1}{2\pi} e^{i\omega s} e^{-i\frac{\omega}{\beta} \hat{y}_3 z_3} G_B(\bar{\mathbf{z}}, \bar{\mathbf{y}}, \bar{\omega}^*) \text{ with } \bar{\omega}^* = \frac{\omega}{\beta} \sqrt{1 - \hat{y}_3^2}$$
(39)

As a result, only a single 2D computation is necessary for each far field point y. This significantly reduces the computational time.

V. An example of application in acoustic analogy

The wave equation appeared in the acoustic analogy is often solved by using the free space Green's function, for instance, the Ffowcs Williams and Hawkings equation. However, with the use of exact Green's function, the far field acoustic solution reduces to a volume integral alone, where in the frequency domain we have

$$\rho'(\mathbf{y},\omega) = \int_{V} T_{ij}(\mathbf{z},\omega) \frac{\partial^{2} \tilde{g}(\mathbf{z},\mathbf{y},\omega,s)}{\partial z_{i} \partial z_{j}} d\mathbf{z}$$
(40)

in which T_{ij} 's are the Lighthill tensor and the geometrical effects of solid boundaries on noise propagation are automatically included in the computed exact Green's function.^{5,6}

In this section, we will show briefly an example of applying (40) to the problem of finding the acoustic radiation generated by a turbulent flow over a circular cylinder. A time dependent RANS (Reynolds Averaged Navier-Stokes) simulation is obtained by using the simulation code CFL3D from NASA Langley Research Center. The free stream Mach number is M=0.2 and the Reynolds number based on the mean flow is Re=10,000. Figure 9 shows the instantaneous flow streamlines and the density contours (in color). Also shown are the contour maps of the maximum T_{ij} 's. The volume integral of (40) is carried out over a region of $0.51 \le r \le 2$ which covers the areas that have the most significant contribution of T_{ij} 's.

Figure 10 shows the density spectrum at far field points as indicated. The tonal variation as a result of the vortex shedding is clearly visible. The fundamental frequency is at Strouhal number fD/U=0.2239. Figure 11 shows the directivity of the acoustic radiation at the fundamental and the first harmonic frequencies. The radiation pattern at the fundamental frequency closely resembles that of a dipole indicated in dashed lines.

VI. Conclusions

A spectral collocation boundary element method has been presented for computing the exact Green's function in the frequency domain. Numerical examples showed an exponential rate of convergence. It is also demonstrated that the use of high order basis function increases the accuracy of the spatial double divergence of the Green's function for field points close to the solid boundaries. In addition, we have showed that the Green's function for a three dimensional point source can be synthesized by the two-dimensional solutions where the Fourier inverse integral is to be evaluated by high order quadratures. Finally, an example of applying the exact Green's function to the noise generation by a flow over a circular cylinder is presented. The predicted far field directivity shows expected dipole pattern.

Acknowledgement: This work is supported by a grant from NASA Langley Research Center, NAG1-03037. The technical monitor is Dr. Mehdi R. Khorrami.

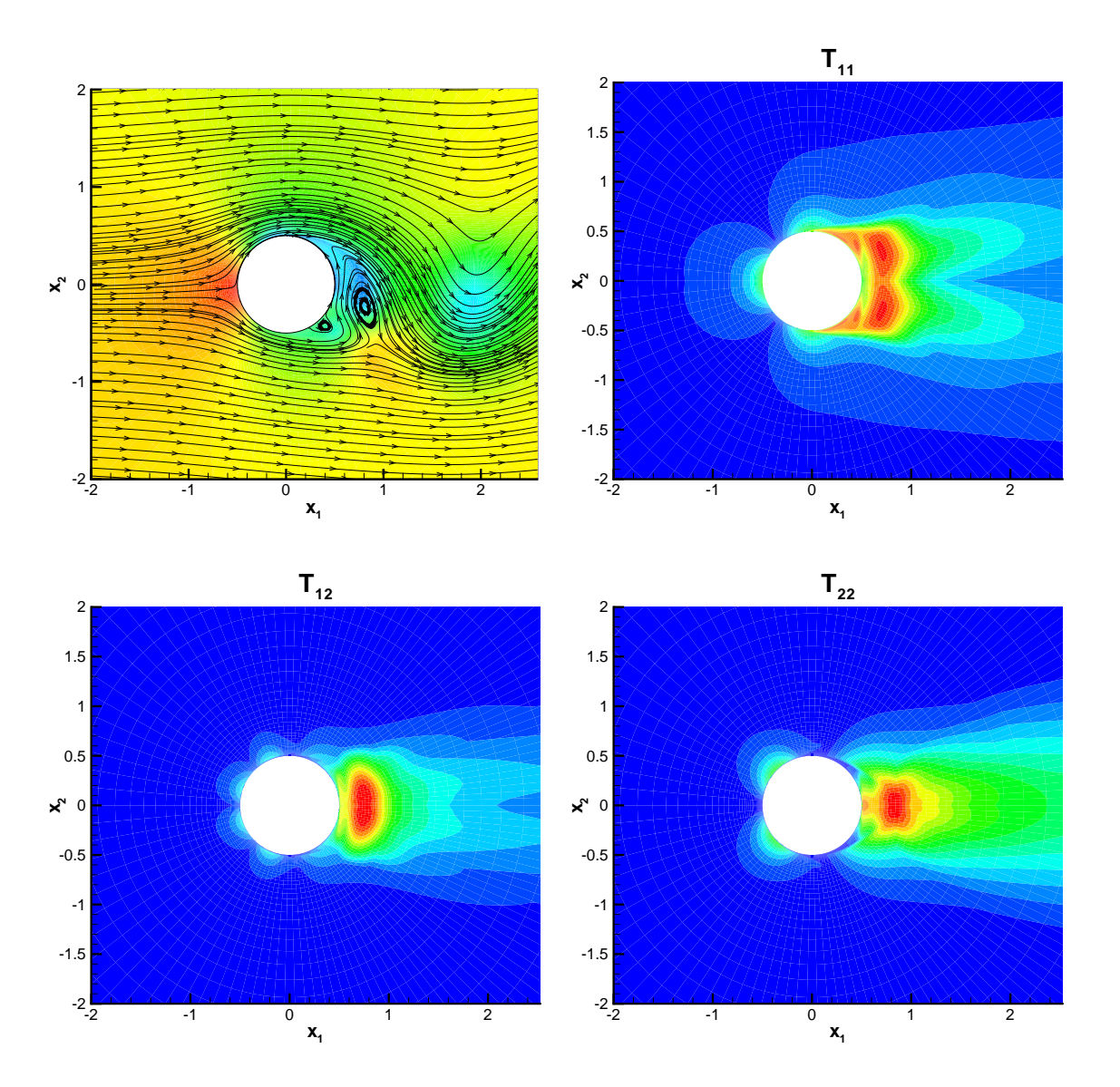


Figure 9. Instantaneous Streamlines and density contours (top left). Also shown are the contours of maximum T_{ij} .

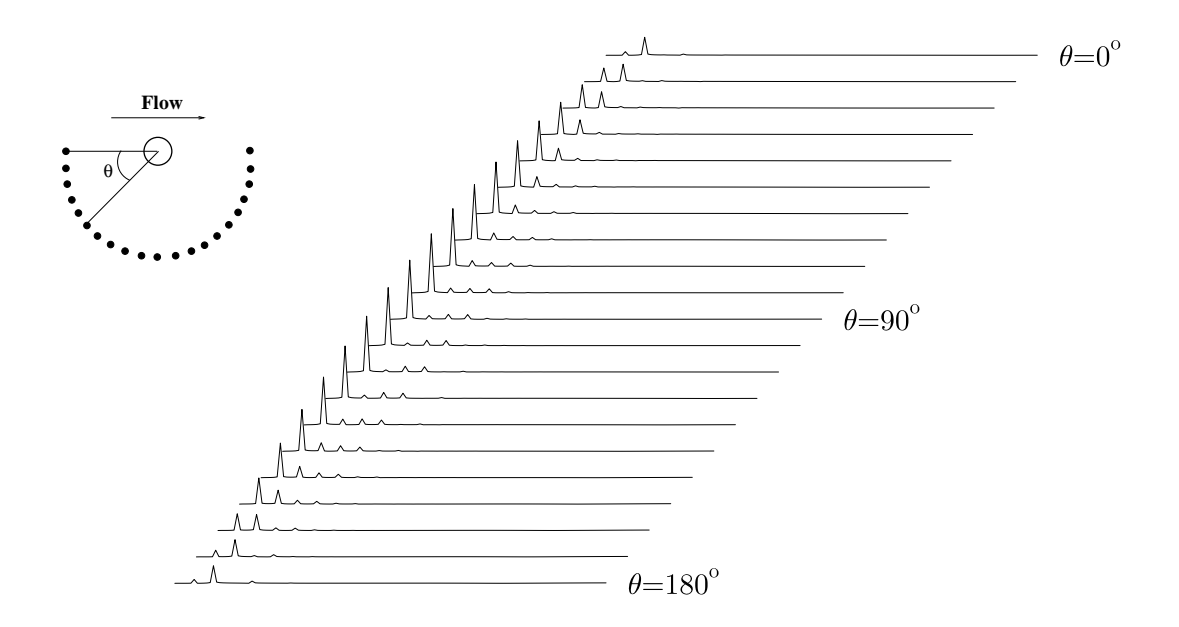


Figure 10. Spectrum of density fluctuation at r=20. Angle θ is measured from the forward direction.

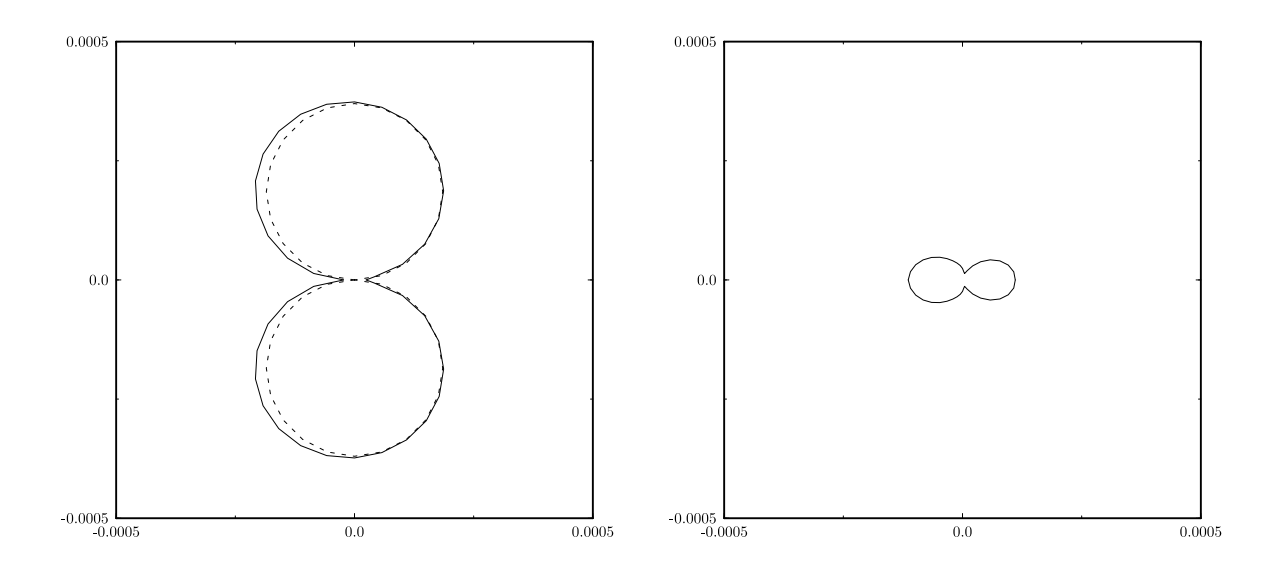


Figure 11. Directivity of the far field density at the fundamental frequency (left) and its harmonic frequency (right). The dotted line indicates the dipole directivity.

Appendix: basis functions

The basis functions are

$$\phi_n(t) = T_n(2t - 1)$$

where $T_n(\xi)$ is the Chebyshev polynomial

$$T_n(\xi) = \cos(n \arccos \xi)$$

The collocation points are the Gauss-Chebyshev points:

$$t_{\ell} = \frac{\xi_{\ell} + 1}{2}, \xi_{\ell} = \cos\left(\frac{2\ell + 1}{2P + 2}\pi\right), \ell = 0, 1, 2, ..., P$$

References

- ¹A. Agarwal and P. J. Morris, 'Broad band noise from the unsteady fbw in a slat cove', AIAA paper 2004-0854, 2004
- ²J. H. Casper, D. P. Lockard, M. R. Khorrami and C. L. Streett, 'Investigation of volumetric sources in airframe noise simulation', AIAA paper 2004-2805, 2004
- ³M. Choudhari, M. R. Khorrami, D. P. Lockard, H. L. Atkins and G. M. Lilley, 'Slat cove noise modeling: A posteriori analysis of unsteady RANS simulations, AIAA paper 2002-2468, 2002.
- ⁴L. B. Felsen and N. Marcuvitz, Radiation and scattering of waves, Prentice-Hall, 1973.
- ⁵J. E. Ffowcs Williams and L. H. Hall, "Aerodynamic sound generation by turbulent fbw in the vicinity of a scattered half plane", Journal of Fluid Mechanics, Vol. 40, 657-670, 1970.
- ⁶M. E. Goldstein, Aeroacoustics, McGraw-Hill, 1976.
- ⁷Y. P. Guo, "Application of the Ffowcs Williams/ Hawkings equation to two-dimensional problems", Journal of Fluid Mechanics, Vol. 403, 201-221, 2000.
- ⁸F. Q. Hu, "A spectral boundary integral equation method for the 2D Helmholtz equation", Journal of Computational Physics, Vol. 120, 340-347, 1995.
- ⁹L. A. de Lacerda, L. C. Wrobel and W. J. Mansur, "A boundary element integral formulation for two-dimensional acoustic radiation in a subsonic uniform fbw", Journal of Acoust. Soc. Am., Vol.100, 98-107, 1996.
- ¹⁰D. P. Lockard, "An efficient, two-dimensional implementation of the Ffowcs Williams and Hawkings equation", Journal of Sound and Vibration, Vol. 229, 897-911, 2000
- ¹¹E. Manoha, G. Elias, B. Troff and P. Sagaut, "Towards the use of Boundary Element Method in computational aeroacoustics", AIAA paper 99-1980, 1999.
- ¹²M. R. Khorrami, M. Choudhari, B. A. Singer, D. P. Lockard and C. L. Streett, 'In search of the physics: the interplay of experiment and computation in slat aeroacoustics', AIAA paper 2003-0980, 2003.
- ¹³J. S. D. Ostertag, A. Celic and S. Wagner, "Trailing-edge noise prediction by SATIN on the basis of steady RANS solutions", AIAA paper 2002-2471, 2002.
- ¹⁴A. Tadeu, P. Santos and J. Antonio, "Amplification of elastic wave due to a point source in the presence of complex surface topography", Computers and Structures, vol. 79, 1697-1712, 2001.
- ¹⁵T. W. Wu and L. Lee, "A direct boundary integral formulation for acoustic radiation in a subsonic uniform fbw", Journal of Sound and Vibration, Vol. 175, No.1, 51-63, 1994.